Atomic manipulation of in-gap states in the β-Bi_2Pd superconductor

Cristina Mier,[1,*] Jiyoon Hwang,[2,3,*] Jinkyung Kim,[2,3] Yujeong Bae,[2,3] Fuyuki Nabeshima,[4] Yoshinori Imai,[4,5] Atsutaka Maeda,[4] Nicolás Lorente,[1,6,†] Andreas Heinrich,[2,3,‡] and Deung-Jang Choi[1,6,7,§]

[1]*Centro de Física de Materiales, MPC (CSIC-UPV/EHU), 20018 Donostia-San Sebastián, Spain*
[2]*Center for Quantum Nanoscience, Institute for Basic Science, Seoul 03760, South Korea*
[3]*Department of Physics, Ewha Womans University, Seoul 03760, South Korea*
[4]*Department of Basic Science, University of Tokyo, Meguro, Tokyo 153-8902, Japan*
[5]*Department of Physics, Graduate School of Science, Tohoku University, Sendai, Miyagi 980-8578, Japan*
[6]*Donostia International Physics Center, 20018 Donostia-San Sebastián, Spain*
[7]*Ikerbasque, Basque Foundation for Science, 48013 Bilbao, Spain*

(Received 6 May 2021; accepted 25 June 2021; published 6 July 2021)

Electronic states in the gap of a superconductor inherit intriguing many-body properties from the superconductor. Here, we create these in-gap states by manipulating Cr atomic chains on the β-Bi_2Pd superconductor. We find that the topological properties of the in-gap states can greatly vary depending on the crafted spin chain. These systems make an ideal platform for nontrivial topological phases because of the large atom-superconductor interactions and the existence of a large Rashba coupling at the Bi-terminated surface. We study two spin chains, one with atoms two lattice parameters apart and one with $\sqrt{2}$ lattice parameters. Of these, only the second one is in a topologically nontrivial phase, in agreement with the spin interactions for this geometry.

DOI: 10.1103/PhysRevB.104.045406

I. INTRODUCTION

The scanning tunneling microscope (STM) permits unprecedented control at the atomic level [1]. Since the early days of STMs, atoms have been moved, unveiling matter on the atomic scale [2–6]. Atoms involve interactions that can have a profound impact on the electronic properties of host substrates; as such, designing atomic structures can lead to creating new quantum states [7]. Magnetic atoms strongly modify the low-energy electronic properties of superconductors. This modification is due to the appearance of *in-gap* states caused by the weakening of the Cooper-pair binding. These in-gap states are usually called Yu-Shiba-Rusinov (YSR) states [8–10]. Recently, interest in in-gap states has increased due to the suggestion of *topological* edge states appearing on chains of magnetic impurities on superconductors [11–18]. These zero-energy edge states imply the presence of a topological superconducting phase. The zero-energy edge states are Majorana bound states (MBSs) with nontrivial exchange transformations. Braiding of MBSs is at the core of current proposals regarding topological quantum computation [19,20].

The STM has become a major tool in the study of MBSs [14–17,21,22]. Indeed, its spectroscopic capabilities render it unique for revealing in-gap states, granting access to unrivaled energy and space resolutions. Recently, the spatial distribution of in-gap states was shown and used to infer new properties of the states themselves [23–25]. The aforementioned STM manipulation can be used to create atomically precise spin chains on superconductors [17,18,26]. The new in-gap states evolve into bands and open gaps displaying new forms of superconductivity [11–13,27]. This evolution proves the complexity of the induced electronic structure. Each added impurity locally creates a few states in the superconducting gap. As the number of impurities grows, the gap *fills* up with new quasiparticle states.

The study of impurity dimers illustrates the initial steps of in-gap bands [28–33]. The quasiparticle states themselves are difficult to describe. In the Bogoliubov–de Gennes approximation, the quasiparticle states are taken as electron and hole superpositions despite violating particle-number conservation. Furthermore, the quasiparticle states are spin polarized [34,35], which has important implications for the way the in-gap states hybridize [28]. In particular, the resulting states reflect the spin ordering of the magnetic impurities [31]. However, recent work suggests that in the presence of strong Rashba coupling, it is difficult to make a conclusion about the actual spin orientation of the impurities by studying the in-gap states [32].

Here, we study atomic spin chains of Cr adsorbed on the hollow sites of β-Bi_2Pd and grown along the two main surface directions, $\langle 100\rangle$ and $\langle 110\rangle$ for the Bi-terminated [001] surface, using a home-built dilution fridge STM [36]. By doing so, we are choosing two starkly different spin orientations for the chain ground state, as concluded in Ref. [31]. Dimers along the $\langle 100\rangle$ direction with a Cr-Cr distance of two unit cells ($2a$, where a is the surface lattice parameter) present antiferromagnetic (AF) coupling of their $5\mu_B$ magnetic

*These authors contributed equally to this work.
†nicolas.lorente@ehu.eus
‡heinrich.andreas@qns.science
§djchoi@dipc.org

moments [31]. Dimers along the ⟨110⟩ direction are $\sqrt{2}a$ apart, and they are instead ferromagnetically (FM) coupled. Here, we compare dimers, trimers, and tetramers of these two types of chains and conclude that the $\sqrt{2}a - \langle 110\rangle$ chains are indeed FM coupled by comparing then with model calculations of spin chains solving the Bogoliubov–de Gennes equations [28,31]. As clearly seen in this work, the gap closes rapidly for the $\sqrt{2}a - \langle 110\rangle$ chains; however, the $2a - \langle 100\rangle$ chains maintain an almost constant gap for chains as long as 12 Cr atoms. This difference has important implications for the possibility of engineering topological phases on the β-Bi_2Pd superconductor.

II. METHODS

A. Sample preparation and STM characterization

The β-Bi_2Pd crystal was fabricated by the method written in Ref. [37]. The chosen sample showed a T_c of 5.2 K. The Bi-terminated surface of the β-Bi_2Pd crystal was prepared by cleavage *in situ* [31]. Cr atoms were deposited onto a precooled β-Bi_2Pd surface at a temperature $T \leqslant 20$ K to have single isolated atoms. The experimental data were taken using a home-built dilution fridge STM at $T = 30$ mK and in ultrahigh vacuum at the IBS Center for Quantum Nanoscience [36]. The very low temperature leads to a negligible thermal smearing granting a resolution higher than the one obtained by a superconducting tip [38–40]. We used a metallic PtIr tip that permitted us to use the differential conductance dI/dV as a direct measurement of the density of states of the substrate (refer to the Supplemental Material [41] for more details). The conductance was measured using a lock-in amplifier with an AC modulation bias of 30 μV and a frequency of 330 Hz.

Lateral atomic manipulation was achieved by approaching one side of a selected atom with the STM tip to reach junction resistances on the order of a few tens of kilohms (typically, 3 mV and tens of nanoamperes). Then the STM tip was laterally moved to drag the atom to a desired position with the feedback loop open.

B. Theory

We model the Cr spin chain in the dilute spin chain limit [13] because density-functional-theory (DFT) calculations show that no Cr d states lie at the Fermi energy, preventing charge transfer processes [31]. In this framework, we solve a spin chain using Green's functions for the superconductor in the Nambu basis set [42,43]. We add a Rashba term to the Hamiltonian expressed in the local basis. The resulting density of states corresponds to the Bogoliubov–de Gennes states of a BCS superconductor in the presence of an array of classical spins and subject to the strong Rashba interaction of the Bi-terminated surface.

The Fermi velocity entering the superconductor's Green's function [42,43] is taken to be 0.15 (Hartree atomic units $\hbar = m = e = 1$), and the Dynes parameter [44] controlling the width of the superconducting quasiparticle peaks is 0.05 meV. The small Dynes parameter leads to peaks in the density of states (DOS) sharper than the experimental ones but helps with the visualization of the evolution of in-gap states with the number of Cr atoms. β-Bi_2Pd is an s-wave superconductor that can be well accounted for by a single gap [37,45] $\Delta = 0.76$ meV. For the normal metal DOS, we use $N = 0.037$/eV, which is 5 times larger than the corresponding N for a free-electron metal with a Fermi velocity of 0.15 a.u., in order to capture the five electrons of the Bi valence shell. The Hamiltonian taking into account the superconductor is

$$\hat{H}_{\mathrm{BCS}} = \xi_k \tau_3 \sigma_0 + \Delta \tau_2 \sigma_2, \tag{1}$$

where σ_i (τ_i) are the Pauli matrices acting on the spin (particle) sectors, with σ_0 (τ_0) being the 2×2 identity matrix and the matrix product being a tensor one. ξ_k is the energy from the Fermi level ($\xi_k = \epsilon_k - E_F$); the previous Hamiltonian is written in the four-dimensional Nambu basis: $\Psi = (\hat{c}_\uparrow, \hat{c}_\downarrow, \hat{c}_\uparrow^\dagger, \hat{c}_\downarrow^\dagger)^T$.

To model the experimental system, we add the Hamiltonian describing the magnetic impurities [42,43]. To do this, we change to a tight-binding basis, assuming a single, very compact, atomic orbital per site. Additionally, the interactions with the magnetic impurity are assumed to be strictly localized to the site where the impurity is sitting [13]. The Hamiltonian is then

$$\hat{H} = \hat{H}_{\mathrm{BCS}} + \hat{H}_{\mathrm{impurity}} = \hat{H}_{\mathrm{BCS}} + \sum_j^N (U_j \tau_3 \sigma_0 + J_j \vec{S}_j \cdot \vec{\alpha}), \tag{2}$$

with $\vec{\alpha} = \frac{1+\tau_3}{2}\vec{\sigma} + \frac{1-\tau_3}{2}\sigma_2 \vec{\sigma} \sigma_2$, where $\vec{\sigma}$ is the spin operator [9]. This Hamiltonian describes a BCS superconductor and the interaction between its electrons and N extra impurities. The interaction contains an exchange coupling, with strength J_j, and a nonmagnetic potential scattering term U_j per impurity j. We will use the same impurity species, Cr, and assume that the impurities are equivalent regardless of their adsorption site and spin chain in order to study the system's evolution with the number of atoms in the spin chains. $\vec{S}_j = (S_{j,x}, S_{j,y}, S_{j,z}) = S(\sin\theta_j \cos\phi_j, \sin\theta_j \sin\phi_j, \cos\theta_j)$ is the spin of atom j considered to be a classical spin and hence not an operator. The local term U_j describes a scalar potential acting on the substrate's electron. It is responsible for the potential scattering term produced by the impurity. In the case of a charged impurity, U_j is mainly given by the Coulomb interaction between the total charge of the impurity and the charge of the substrate's electron. The potential scattering that explains the electron-hole asymmetry of the YSR bands is taken as $U_j = 5.5$ eV. The values for the Kondo exchange coupling J_j are about 2 eV, as estimated from fittings to single-Cr YSR states [31].

The Hamiltonian is completed by a Rashba term:

$$\hat{H}_{\mathrm{Rashba}} = i\frac{\alpha_R}{2a} \sum_{i,j,\alpha,\beta} [\hat{c}^\dagger_{i+1,j,\alpha}(\sigma_2)_{\alpha,\beta}\hat{c}_{i,j,\beta} - \hat{c}^\dagger_{i,j+1,\alpha}(\sigma_1)_{\alpha,\beta}\hat{c}_{i,j,\beta} + \mathrm{H.c.}], \tag{3}$$

where α, β are spin indexes. The interaction couples spins on nearest-neighbor sites. The lattice parameter of the substrate is a, and the factor of $2a$ comes from a finite-difference scheme to obtain the above discretized version of the Rashba interaction. For the case of β-Bi_2Pd, we use a large Rashba coupling, $\alpha_R \approx 1.8$ eV Å, which comes from our DFT calculations and

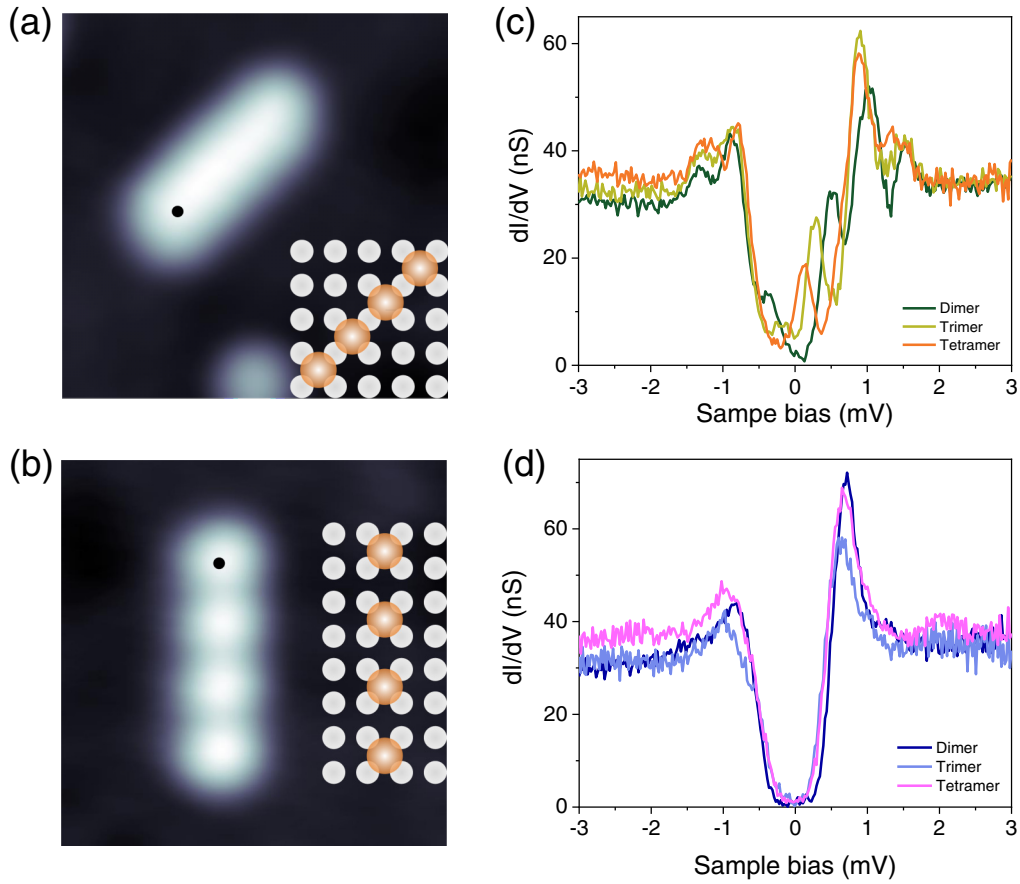

FIG. 1. Chromium chains built on the β-Bi_2Pd surface by atomic manipulation. Topographic images of tetramer chains (a) $\sqrt{2}a - \langle 110\rangle$ and (b) $2a - \langle 100\rangle$ unit cells apart (100 mV, 10 pA, 4×4 nm^2). The insets show the atomic geometry of the tetramer nanostructures. The corresponding differential conductance is measured at the end atom (black dot) from the dimer to trimer to tetramer in tetramer chains (c) $\sqrt{2}$ unit cells apart and (d) 2 unit cells apart. $T = 30$ mK; AC modulation bias is 30 μV.

is in agreement with the couplings of Bi-terminated surfaces [46].

The local or projected DOS (PDOS) is computed over every local orbital i of the basis using

$$\rho(i,\omega) = -\frac{1}{\pi}\mathrm{Im}\big[G^{1,1}_{i,i}(\omega) + G^{4,4}_{i,i}(-\omega)\big], \tag{4}$$

where $G^{\nu,\mu}_{ii}$ is the resulting Green's function evaluated on orbital i for the Nambu components ν and μ by solving Dyson's equation:

$$\hat{G} = \big[\hat{G}^{-1}_{\mathrm{BCS}} - \hat{H}_I\big]^{-1}, \tag{5}$$

where $\hat{G}_{\mathrm{BCS}}$ is the retarded Green's operator for the BCS Hamiltonian from Eq. (1) and $\hat{H}_I = \hat{H}_{\mathrm{impurity}} + \hat{H}_{\mathrm{Rashba}}$.

The DFT calculations were performed using the VASP code [47]. The β-Bi_2Pd slab was optimized using the Perdew-Burke-Ernzerhof form of the generalized gradient approximation [48], following the calculations of Ref. [31]. For more details, see the Supplemental Material [41].

III. RESULTS AND DISCUSSION

The dI/dV over a single Cr adatom yields a single YSR state given by peaks at $V = \pm 0.35$ mV (see Refs. [31,41]). By lateral atomic manipulation, we place Cr atoms to create linear $\sqrt{2}a - \langle 110\rangle$ or $2a - \langle 100\rangle$ chains. Figures 1(a) and 1(b) show constant-current images of the two tetramer chains. The chain in Fig. 1(a) corresponds to the $\sqrt{2}a - \langle 110\rangle$ tetramer as depicted in the inset; the one in Fig. 1(b) is the $2a - \langle 100\rangle$ tetramer. As the chain is made larger, misplacing a Cr atom becomes more common. Indeed, error-free $\sqrt{2}a - \langle 110\rangle$ spaced nanostructures were difficult to obtain, while $2a - \langle 100\rangle$ chains are easier to manipulate. The reason lies in the chemistry of the chains. For the more compact chains, the affinity of Cr atoms for certain conformations leads to nonlinear arrangements. The less compact $2a - \langle 100\rangle$ chain is easier to fabricate by single-atom manipulation because the atoms do not approach each other as much, and hence, cluster formation is much less common.

Our DFT calculations yield a coherent picture with the experiment. The Cr atoms are preferentially adsorbed on the hollow sites of the Bi-rich surface [31], and the Cr-Cr interactions in the chains are mediated by a single Bi atom in the $\sqrt{2}a - \langle 110\rangle$ chains or a square of four Bi atoms in the $2a - \langle 100\rangle$ chains. Short $1a - \langle 100\rangle$ chains can also be obtained, but the structures easily become clusters due to the Cr-Cr interaction. The $\sqrt{2}a - \langle 110\rangle$ dimer is 249 meV less stable than the $1a - \langle 100\rangle$ dimer. As a consequence,

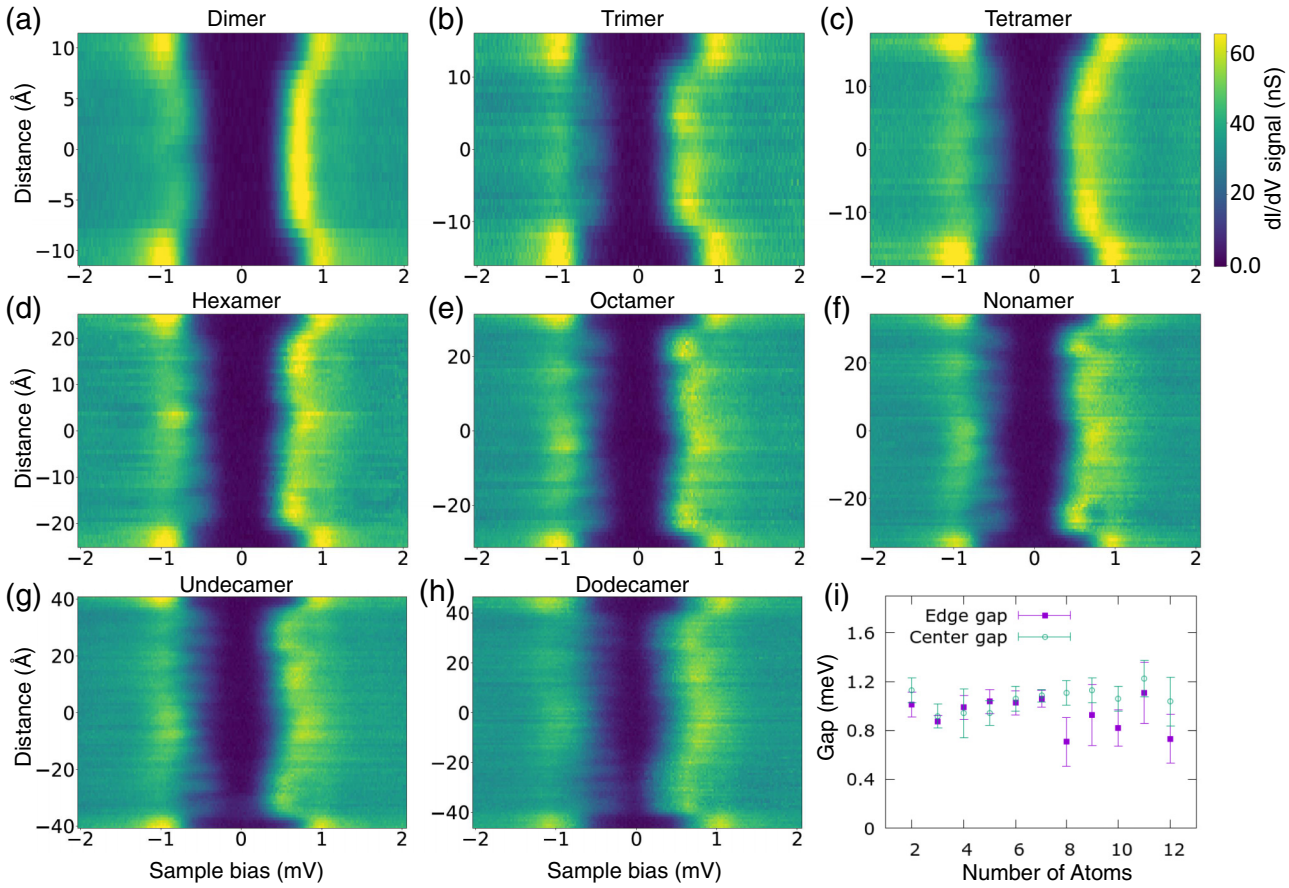

FIG. 2. Differential conductance measured along Cr_n $2a - \langle 100 \rangle$ chains with $n = 2$ in (a), $n = 3$ in (b), $n = 4$ in (c), $n = 6$ in (d), $n = 8$ in (e), $n = 9$ in (f), $n = 11$ in (g), and $n = 12$ in (h). The x axis represents the sample bias; the y axis displays the distances over the chain. The color code gives the intensity of the differential conductance. The smallest gap in the system, defined as the distance between the lower quasiparticle peak and the highest quasihole peak, is plotted in (i). In the absence of Cr atoms, the gap corresponds to 2Δ, where $\Delta = 0.76$ meV for β-Bi_2Pd. The gap has been obtained at an edge atom or at the center of the spin chain.

shifting a single Cr atom towards another Cr to reach the short $\sqrt{2}a$ distance likely produces a $1a - \langle 100 \rangle$ dimer. This stacking error becomes more likely as the chain is manipulated more times to make it longer. The $2a - \langle 100 \rangle$ dimer is only 30 meV less stable than the $\sqrt{2}a - \langle 110 \rangle$ dimer. But, still, the interactions between atoms for the larger Cr-Cr distance, $2a - \langle 100 \rangle$ chains, are weaker, resulting in easier manipulation to build longer chains. Indeed, the bottom-up approach of chain building is difficult on many other substrates [49]. Recent experiments showed long Mn chains built in a similarly compact geometry but on a Nb(110) substrate, also giving rise to topological in-gap behavior [50,51].

Once the chains are built, the differential conductance dI/dV, as a function of bias V and surface position, is an extraordinary probe of the electronic properties of the new systems. Figures 1(c) and 1(d) show dI/dV spectra measured at $T = 30$ mK for the dimer, trimer, and tetramer of $\sqrt{2}a - \langle 110 \rangle$ and $2a - \langle 100 \rangle$ types, respectively. The dI/dV spectra are taken at an edge atom [black dots in Figs. 1(a) and 1(b)]. The two sets [Figs. 1(c) and 1(d)] are starkly in contrast. Figure 1(c) clearly shows an in-gap state that is shifting towards zero bias as the chain gets longer. With opposite behavior, Fig. 1(d) shows no clear in-gap state and a well-formed gap. Furthermore, the gap for the dimer is larger, but the trimer and tetramer show similar gaps, pointing at a rapid stabilization of the gap with the chain size. The extra peaks around ± 1.5 mV on the outside of the gap appear occasionally, depending on the tip. The in-gap states are not affected by the appearance of these higher-energy structures and hence by the actual configuration of the tip.

The in-gap states of the $\sqrt{2}a - \langle 110 \rangle$ dimer agree well with a model of two FM aligned spins. When the magnetic moments are coupled antiferromagnetically, the in-gap state approaches the individual Cr adatom YSR states [31], behavior that explains the apparent absence of YSR states in Fig. 1(d). The presence of YSR in-gap states can be revealed by studying the spatial distribution of the differential conductance along the two types of chains. Figures 2, 3, and 4 show the dI/dV in a color scale (bright yellow corresponds to larger conductance, and dark blue represents zero conductance) along the chain, with the y axis (in angstrom) showing the distances over the chain and the x axis (in millivolts) showing the STM junction's bias.

A. $2a - \langle 100 \rangle$ spin chains

Figure 2 shows the results for the $2a - \langle 100 \rangle$ spin chains. As seen in Fig. 1(d), we find no obvious structure in the gap in any of the studied chains. A closer look reveals atomic

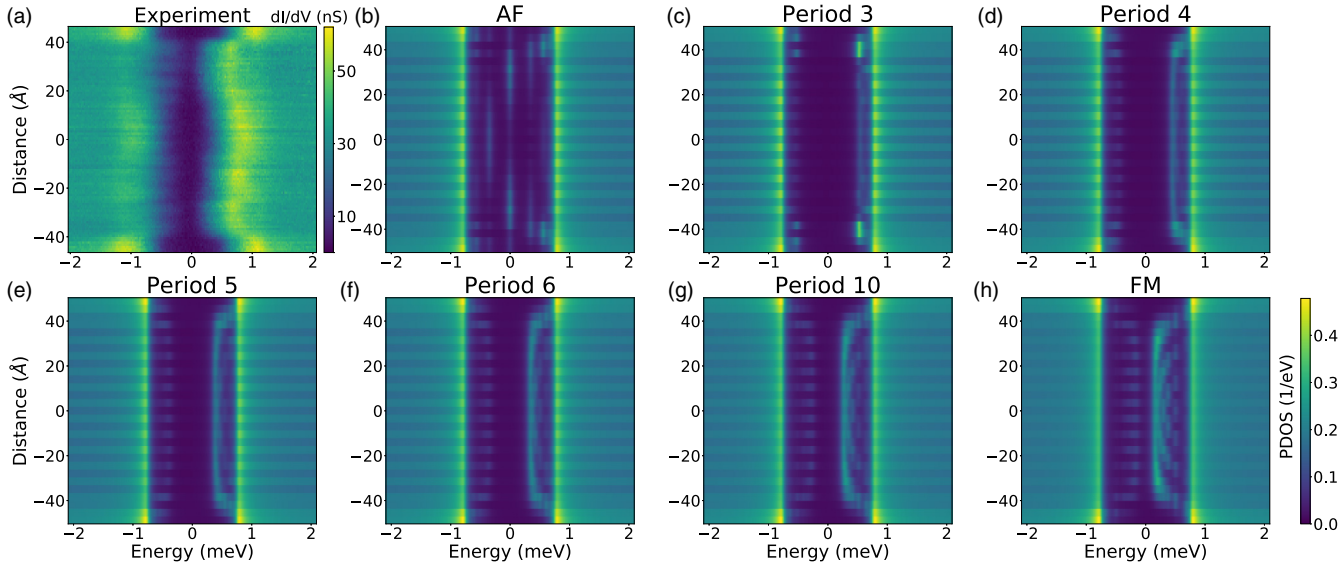

FIG. 3. Differential conductance along a Cr_{12} $2a - \langle 100 \rangle$ chain comparing (a) the experimental result and (b)–(h) the computed PDOSs for different noncollinear spin arrangements. The first case, in (b), is for an antiferromagnetic (AF) arrangement of spins. The spins on nearest-neighbor Cr atoms present a 180° angle. In (c) the angle is 120°, such that a period of three Cr atoms is needed to turn the spin along the chain. The case in (d) corresponds to a period of four atoms or a 90° configuration. For (e), the mutual angle is 72°; for (f), the angle is 60°. In (g), we plot period 10 or the 36° spin angle, and finally, (h) corresponds to the ferromagnetic (FM) case. The best agreement with the measured spectra in (a) corresponds to a noncollinear arrangement with spins forming 120°.

modulations of the quasihole states that match the number of atoms in the chains. The presence of YSR states can be inferred by the profile of the gap. The complete sequence of chains from $n = 2$ to $n = 12$ can be found in the Supplemental Material [41]. All chains roughly show a smaller gap at the edge atoms than at the center of the chain [see Fig. 2(i)]. In the first approximation, the gap is constant with chain length. Beyond eight atoms, the chains show a smaller gap at the edge. However, the closing of the gap is very small and almost constant for longer chains. These data indicate that the YSR states are not able to close the superconducting gap, preventing any topological phase transition.

By computing the PDOS, Eq. (4), we can evaluate the in-gap state spectra and compare them with the experimental data. The $2a - \langle 100 \rangle$ dimer presents excellent agreement between theory and experiment if no Rashba coupling is considered and the dimer spins are coupled antiferromagnetically, as shown in Ref. [31]. In the present work, we have gone a step further by including the spin-orbit Rashba coupling between electronic spins, Eq. (3).

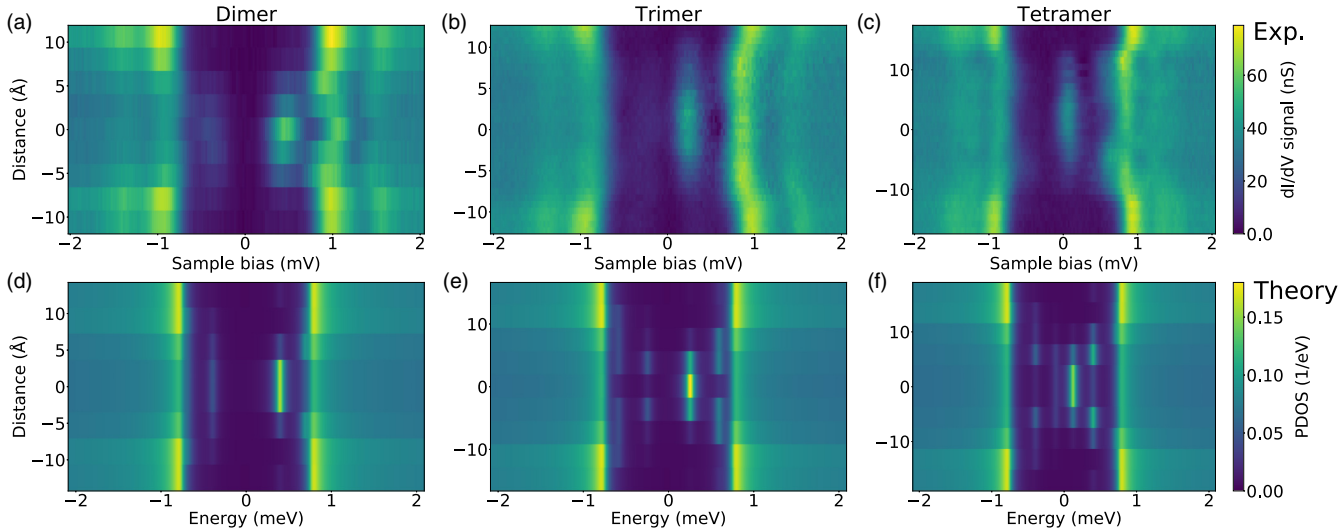

FIG. 4. Experimental differential conductance measured along the Cr adatoms of the $\sqrt{2}a - \langle 110 \rangle$ (a) dimer, (b) trimer, and (c) tetramer chains. The corresponding calculations for the ferromagnetically coupled $\sqrt{2}a - \langle 110 \rangle$ (d) dimer, (e) trimer, and (f) tetramer chains. The color code refers to the PDOS on the different sites of the tight-binding lattice, in this case the one corresponding to the Cr adatoms.

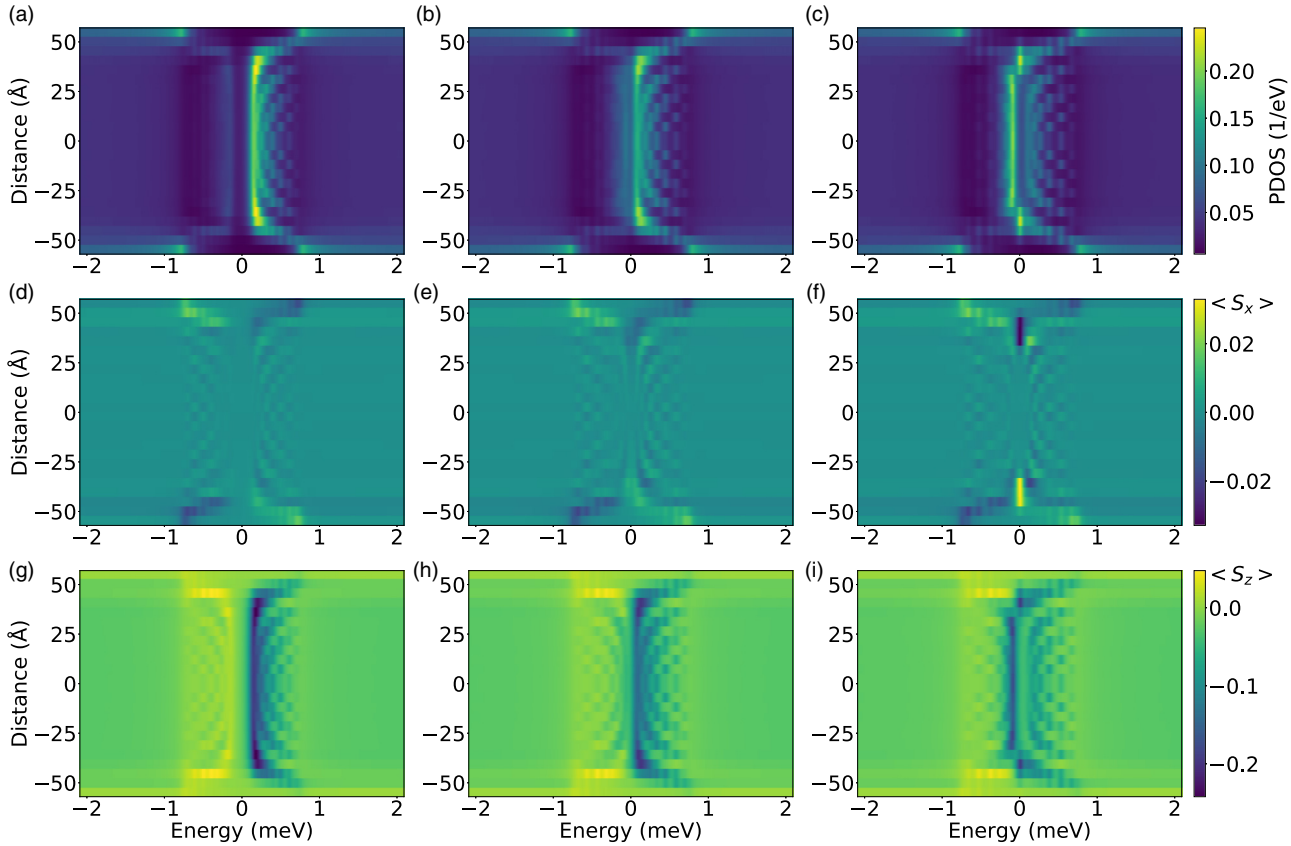

FIG. 5. Topological phase transition induced by increasing the exchange coupling J. The three columns correspond to three different values of the exchange coupling, (a) $J = 2.1$ eV, (b) $J = 2.3$ eV, and (c) $J = 2.5$ eV, for the PDOS showing the quasiparticle states induced by a Cr_{20} $\sqrt{2}a - \langle 110\rangle$ chain. We see that the gap is virtually closed for $J = 2.3$ eV and reopens for $J = 2.5$ eV, displaying the MBS that indicates the change in topological phase of the superconductor. (d)–(f) correspond to the respective values of J and show the transversal spin density $\langle S_x\rangle$ along the chain. We see that $\langle S_x\rangle$ becomes large and of opposite sign only at the two MBSs. Finally, (g)–(i) show the spin density $\langle S_z\rangle$ of the YSR states for the three different couplings. We find that the spin across the gap reverts when the TPT is achieved and the corresponding MBSs have the same well-defined spin.

In the absence of Rashba coupling, the electronic spin is a good quantum number, and the YSR states are spin polarized. The FM ordering between impurity spins leads to YSR states that are also FM ordered, allowing for extended in-gap states. However, AF ordering leads to localized in-gap states that do not disperse. The AF results are in good agreement with the spectra of Fig. 2(a).

When the Rashba coupling is added, the YSR states start mixing between impurities that have opposite spins, leading to splitting of the YSR states and to an important dispersion of the in-gap states [32]. As a consequence, the agreement between theory and experiment worsens. Figure 3 shows the results for a $Cr_{12}2a - \langle 100\rangle$ spin chain. The experimental spectra [Fig. 3(a)] do not match the states of the computed AF configuration [Fig. 3(b)]. However, the agreement improves if noncollinear configurations are used. The spectra in Fig. 3(c) correspond to noncollinear Cr spins forming 120°, which leads to a spin spiral with a periodicity of three atoms. The noncollinearity compensates for the Rashba coupling mixing. The resulting YSR states do not disperse, leading to spectra that compare favorably with the experimental one in Fig. 3(a).

Increasing the noncollinearity leads to smaller angles and larger spiral periods. Figure 3 shows how the gap fills up with states as the Cr spin configuration approaches the FM ordering [Fig. 3(h)].

DFT calculations with spin-orbit coupling yield the lowest energy to the AF ordering, however. Further work is needed to clearly determine the spin configuration of the $2a - \langle 100\rangle$ chains. To this end, spin measurements with a superconducting tip are a recent promising technique [35].

B. $\sqrt{2}a - \langle 110\rangle$ spin chains

Figure 4 presents the dI/dV maps of the $\sqrt{2}a - \langle 110\rangle$ chains (top row) compared to model calculations of the PDOS on the surface sites (bottom row). Figure 4 shows excellent agreement between experiment and theory if the magnetic moments are ferromagnetically coupled, which is also in good agreement with the results of Ref. [31]. The calculations for the YSR structure confirm the FM ordering for Cr atoms sitting along the $\sqrt{2}a - \langle 110\rangle$ hollow sites. Moreover, the magnetic ordering is not altered by adding extra atoms to the dimer.

The data in Fig. 4 permit us to have a clear picture of the in-gap states for the $\sqrt{2}a - \langle 110\rangle$ chains. The dimer presents two YSR bands, one closer to zero energy with a larger

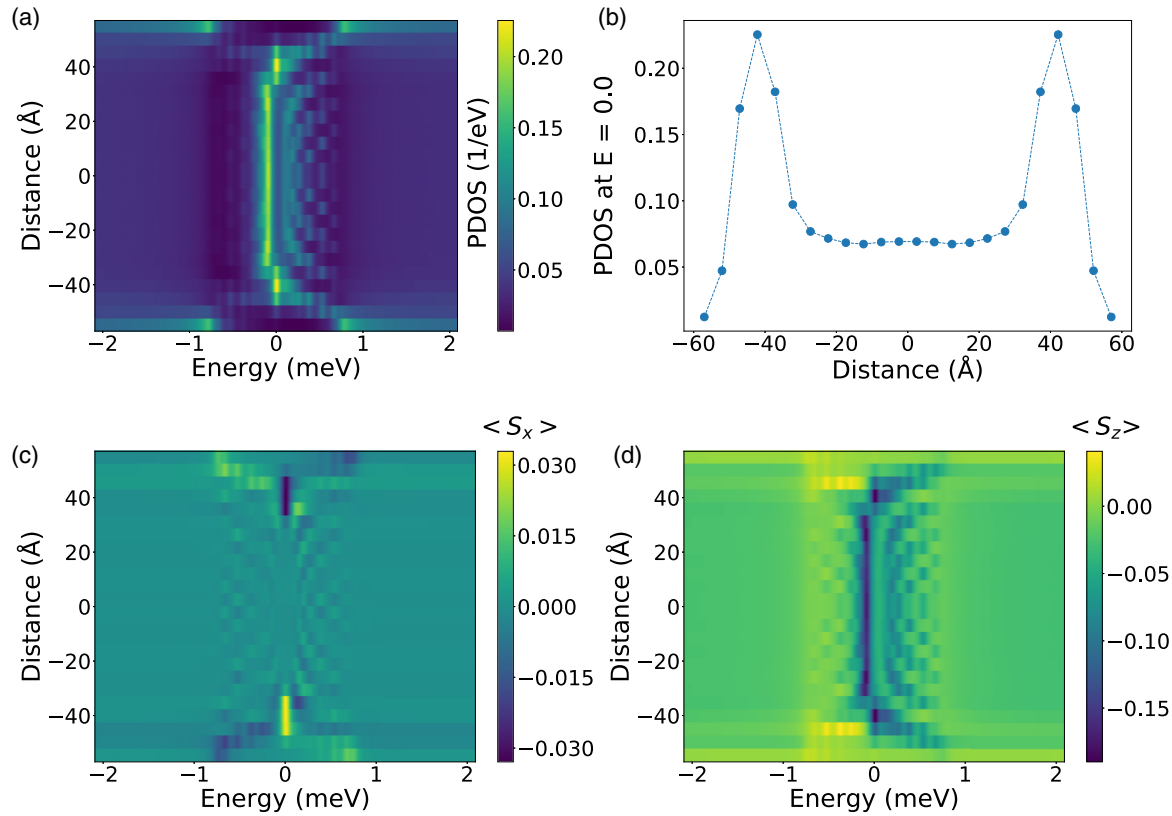

FIG. 6. Majorana bound states in a 20-atom $\sqrt{2}a - \langle 110 \rangle$ Cr spin chain. (a) Color map plotting the PDOS as a function of energy and distance. There is a clear state localized at the edges of the chain and at exactly zero energy. (b) PDOS at zero energy along the 20 Cr chain; x axis is the distance along the Cr chain. The localization of the PDOS to the edges at zero energy spans the four Cr edge atoms, and the PDOS sharply falls beyond. The value of the PDOS between edges reduces as the chain length increases. (c) Color map (dark: negative, light: positive) showing that the transversal spin density $\langle S_x \rangle$ changes sign with the edge, but (d) the spin density component $\langle S_z \rangle$ is the same for both edges. Moreover, these data can be correlated with a clear change in spin sign across the gap as the exchange-interaction value J is increased, which shows the closing and reopening of the gap into the topological phase. All these data signal the presence of a Majorana bound state in a 20-atom $\sqrt{2}a - \langle 110 \rangle$ Cr spin chain.

density of states between the two Cr adatoms and one closer to the quasiparticle continuum with a minimum between the atoms. Adding one more atom to form the trimer shifts the lowest-energy YSR state closer to zero but keeps its overall spatial distribution with a maximum PDOS on the central atom. Furthermore, we find the second band closer to the quasiparticle continuum and, again, with a minimum PDOS over the central point of the chain. We also notice that as in the dimer case, the quasiparticle PDOS presents a reduction and an oscillation along the chain. Finally, the tetramer shifts both bands closer to zero, although largely keeping their spatial distributions. The PDOS at the quasiparticle edge presents the same features as for the dimer and trimer.

In order to match the very fast experimental closing of the gap with the chain length, the Kondo exchange coupling J is increased from $J = 2.0$ eV for the dimer, $J = 2.1$ eV for the trimer, and $J = 2.3$ eV for the tetramer, respectively, in Figs. 4(d)–4(f). This behavior can be rationalized by a possible geometrical and electronic rearrangement of the chain as the spin chain grows in size. The atoms place themselves more symmetrically and closer to the surface, leading to a larger hybridization with the substrate and thus to larger couplings.

The MBSs appear naturally as soon as the exchange coupling J is larger than 2.3 eV. It is interesting to study how the appearance of MBSs takes place as J varies. This is plotted in Fig. 5. The panels are arranged in three columns. Each column corresponds to a different value of J. The first one has $J = 2.1$ eV, the second one has $J = 2.3$ eV, and the third one has $J = 2.5$ eV. The first row plots the PDOS along the chain (y axis) as a function of the quasiparticle energy (x axis). We see the formation of YSR bands already for this 20-atom chain. In the middle of the chain, there is a clear gap in the YSR structure. For small J, this gap is maintained all along the chain; for the larger J, the gap is closed by an edge state that is a MBS, as we shall briefly see. For $J = 2.3$ eV, we see that the lowest-energy bands are still separated by a very small gap, almost closing, and for $J = 2.5$ the gap is well formed again. The closing and reopening of the gap are a necessary condition to change to a topologically nontrivial superconducting band structure.

The second row is the transversal spin density component $\langle S_x \rangle$ along the chain for the same YSR state as above. We see that the values are small and dispersed for $J = 2.1$ and 2.3 eV. For $J = 2.3$ eV the values of $\langle S_x \rangle$ extend all over the superconducting gap, giving the impression of many YSR

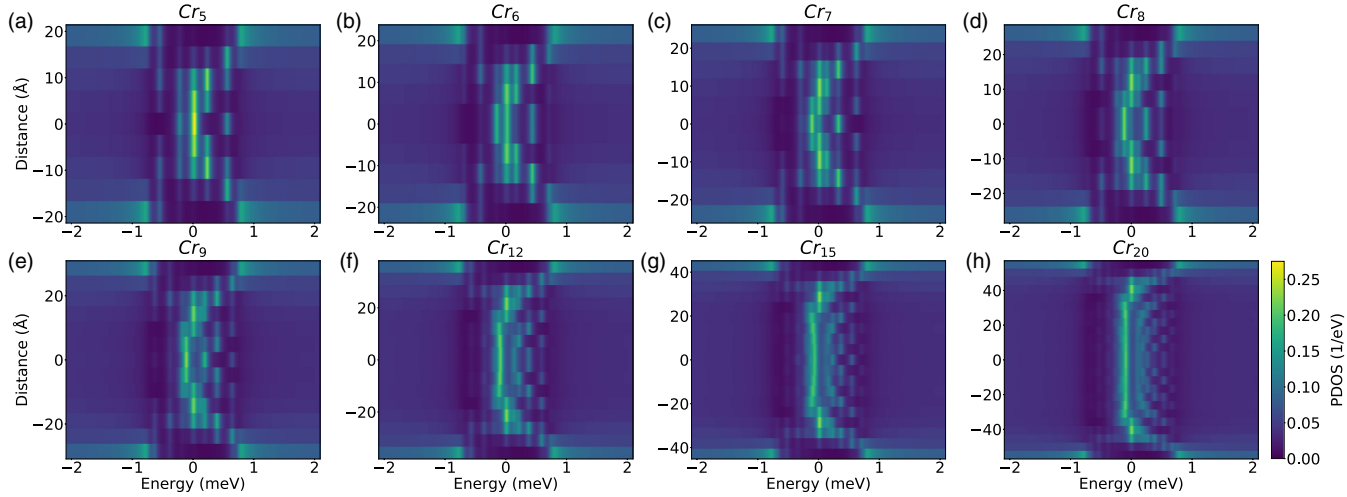

FIG. 7. Cr_n $\sqrt{2}a - \langle 110 \rangle$ chains, with n from 5 to 20, for $J = 2.5$ eV such that the superconductor is in the topological phase. The zero-energy state moves away from the center of the chain to the borders as the chain is increased in size. At fairly low numbers, eight or even seven atoms, the MBSs become clear, and a gap is formed at the center of the chain.

states closing the gap. But $J = 2.5$ eV is very different. The gap in $\langle S_x \rangle$ is again clear, and very sharp values at just the edge states appear and are of opposite sign. This is a clear signature of a MBS [52].

The third row shows the spin $\langle S_z \rangle$ of the YSR states. From the above data, we have evidence that a topological phase transition (TPT) has taken place between $J = 2.1$ eV and $J = 2.5$ eV, with $J = 2.3$ eV being near the closing of the gap. The spin shows it unambiguously. The YSR bands show opposite spin polarizations for their particle and hole components, which is clearly seen across the YSR gap. But the character has changed between $J = 2.1$ eV and $J = 2.5$ eV because the spin polarization is the opposite one. This opposite spin polarization is a clear hallmark of a TPT [53]. The edge states show the same spin polarization as the MBSs [52].

The experimental data show that the gap is almost closed for the tetramer Cr_4 $\sqrt{2}a - \langle 110 \rangle$ spin chain. Closing the gap is a necessary condition for a TPT. Figure 5 clearly shows that the edge states for J larger than 2.3 eV are indeed MBSs and that the TPT takes place somewhere close to 2.3 eV. The change in YSR band character through the TPT is clearly seen in the YSR spin polarization [53]; indeed, the spin inverts across the transition.

Figure 6 shows the calculation of a $Cr_{20}\sqrt{2}a - \langle 110 \rangle$ spin chain with $J = 2.5$ eV. A clear spin-polarized edge state appears, with opposite transversal spin components $\langle S_x \rangle$ on the chain edges showing that indeed MBSs are formed [52]. The number of atoms in the spin chain is decisive, clearly showing MBSs. However, short chains may suffice to prove that indeed the superconductor undergoes a TPT.

For a spin chain in the topological phase, the appearance of the MBSs needs a certain minimum chain size because the MBSs have a certain extension and they overlap for small chains. The consequence is that the zero-energy state becomes localized in the center of the chain, and it is difficult to identify the new superconducting phase as topological.

The behavior of MBSs with the chain's length is shown in Fig. 7 for Cr_n $\sqrt{2}a - \langle 110 \rangle$ chains, with n from 5 to 20. The parameters are the above ones with $J = 2.5$ eV that correspond to the topological phase. In the case of the pentamer, Fig. 7(a) clearly shows a closed gap. We find a zero-energy state for Cr_5 that looks very similar to the experimental (and theoretical) one for Cr_4. The zero-energy state is clearly localized in the center of the chain. As the chain length is increased, the state localizes to the edges. At the same time there is an excitation gap appearing in the center of the chain. For $n = 8$ atoms, it is already possible to clearly differentiate the features of the well-formed MBSs even though the chain is still small and the YSR states present a strong discrete nature. As the length is increased, a clear MBS appears. These calculations imply that Cr_n $\sqrt{2}a - \langle 110 \rangle$ chains on β-Bi_2Pd will clearly show MBSs and topological features at fairly small chains. Indeed, 20 atoms suffice to have an unambiguous topological spin chain.

IV. CONCLUSION

In summary, Cr_n $\sqrt{2}a - \langle 110 \rangle$ spin chains on β-Bi_2Pd show a fast closing of the superconducting gap as the number of atoms in the chain increases. As few as four Cr atoms suffice to have in-gap states closing down the gap. We showed that an eight-atom $\sqrt{2}a - \langle 110 \rangle$ chain may already display all features of MBSs. Our study revealed that the $\sqrt{2}a - \langle 110 \rangle$ Cr spin chain shows ferromagnetic alignment of its spins. The large magnetic moment of Cr plus a sizable Rashba coupling of the β-Bi_2Pd surface lead to the topological phase transition. Increasing the distance between Cr atoms leads to facile atom manipulation that translates in longer chains of Cr atoms on β-Bi_2Pd but at the cost of not reaching a topological phase. Indeed, our measurements show a persistent gap rather constant with chain length for Cr_n $2a - \langle 100 \rangle$, showing that this type of chain will not induce a topological phase transition on the β-Bi_2Pd superconductor. The topological character of the Cr_n $\sqrt{2}a - \langle 110 \rangle$ spin chains reveals the presence of Majorana bound states in our simulations for chains as short as eight atoms.

ACKNOWLEDGMENTS

Financial support from the Spanish MICINN (Projects RTI2018-097895-B-C44 and Excelencia EUR2020-112116), Eusko Jaurlaritza (Project PIBA_2020_1_0017), JSPS KAKENHI (Grants No. JP18K03531 and No. JP19K14651), and the Institute for Basic Science (Grant No. IBS-R027-D1) is gratefully acknowledged.

[1] P. Avouris, Acc. Chem. Res. **28**, 95 (1995).
[2] D. M. Eigler and E. K. Schweizer, Nature (London) **344**, 524 (1990).
[3] J. A. Stroscio and D. M. Eigler, Science **254**, 1319 (1991).
[4] G. Meyer, S. Zöphel, and K. H. Rieder, Appl. Phys. A **63**, 557 (1996).
[5] K. Morgenstern, N. Lorente, and K.-H. Rieder, Phys. Status Solidi B **250**, 1671 (2013).
[6] S. Clair and D. G. de Oteyza, Chem. Rev. **119**, 4717 (2019).
[7] A. A. Khajetoorians, D. Wegner, A. F. Otte, and I. Swart, Nat. Rev. Phys. **1**, 703 (2019).
[8] L. Yu, Acta Phys. Sin. **21**, 75 (1965).
[9] H. Shiba, Prog. Theor. Phys. **40**, 435 (1968).
[10] A. I. Rusinov, Sov. JETP **9**, 85 (1969).
[11] T.-P. Choy, J. M. Edge, A. R. Akhmerov, and C. W. J. Beenakker, Phys. Rev. B **84**, 195442 (2011).
[12] S. Nadj-Perge, I. K. Drozdov, B. A. Bernevig, and A. Yazdani, Phys. Rev. B **88**, 020407(R) (2013).
[13] F. Pientka, L. I. Glazman, and F. von Oppen, Phys. Rev. B **88**, 155420 (2013).
[14] S. Nadj-Perge, I. K. Drozdov, J. Li, H. Chen, S. Jeon, J. Seo, A. H. MacDonald, B. A. Bernevig, and A. Yazdani, Science **346**, 602 (2014).
[15] M. Ruby, F. Pientka, Y. Peng, F. von Oppen, B. W. Heinrich, and K. J. Franke, Phys. Rev. Lett. **115**, 197204 (2015).
[16] R. Pawlak, M. Kisiel, J. Klinovaja, T. Meier, S. Kawai, T. Glatzel, D. Loss, and E. Meyer, npj Quantum Inf. **2**, 16035 (2016).
[17] H. Kim, A. Palacio-Morales, T. Posske, L. Rózsa, K. Palotás, L. Szunyogh, M. Thorwart, and R. Wiesendanger, Sci. Adv. **4**, eaar5251 (2018).
[18] D.-J. Choi, N. Lorente, J. Wiebe, K. von Bergmann, A. F. Otte, and A. J. Heinrich, Rev. Mod. Phys. **91**, 041001 (2019).
[19] A. Kitaev, Ann. Phys. (NY) **303**, 2 (2003).
[20] C. Nayak, S. H. Simon, A. Stern, M. Freedman, and S. Das Sarma, Rev. Mod. Phys. **80**, 1083 (2008).
[21] A. Palacio-Morales, E. Mascot, S. Cocklin, H. Kim, S. Rachel, D. K. Morr, and R. Wiesendanger, Sci. Adv. **5**, eaav6600 (2019).
[22] B. Jäck, Y. Xie, and A. Yazdani, arXiv:2103.13210.
[23] G. C. Ménard, S. Guissart, C. Brun, S. Pons, V. S. Stolyarov, F. Debontridder, M. V. Leclerc, E. Janod, L. Cario, D. Roditchev, P. Simon, and T. Cren, Nat. Phys. **11**, 1013 (2015).
[24] M. Ruby, Y. Peng, F. von Oppen, B. W. Heinrich, and K. J. Franke, Phys. Rev. Lett. **117**, 186801 (2016).
[25] D.-J. Choi, C. Rubio-Verdú, J. de Bruijckere, M. M. Ugeda, N. Lorente, and J. I. Pascual, Nat. Commun. **8**, 15175 (2017).
[26] A. Kamlapure, L. Cornils, J. Wiebe, and R. Wiesendanger, Nat. Commun. **9**, 3253 (2018).
[27] Y. Peng, F. Pientka, L. I. Glazman, and F. von Oppen, Phys. Rev. Lett. **114**, 106801 (2015).
[28] M. E. Flatté and D. E. Reynolds, Phys. Rev. B **61**, 14810 (2000).
[29] S. Kezilebieke, M. Dvorak, T. Ojanen, and P. Liljeroth, Nano Lett. **18**, 2311 (2018).
[30] M. Ruby, B. W. Heinrich, Y. Peng, F. von Oppen, and K. J. Franke, Phys. Rev. Lett. **120**, 156803 (2018).
[31] D.-J. Choi, C. G. Fernández, E. Herrera, C. Rubio-Verdú, M. M. Ugeda, I. Guillamón, H. Suderow, J. I. Pascual, and N. Lorente, Phys. Rev. Lett. **120**, 167001 (2018).
[32] P. Beck, L. Schneider, L. Rózsa, K. Palotás, A. Lászlóffy, L. Szunyogh, J. Wiebe, and R. Wiesendanger, Nat. Commun. **12**, 2040 (2021).
[33] H. Ding, Y. Hu, M. T. Randeria, S. Hoffman, O. Deb, J. Klinovaja, D. Loss, and A. Yazdani, Proc. Natl. Acad. Sci. U.S.A. **118**, e2024837118 (2021).
[34] L. Cornils, A. Kamlapure, L. Zhou, S. Pradhan, A. A. Khajetoorians, J. Fransson, J. Wiebe, and R. Wiesendanger, Phys. Rev. Lett. **119**, 197002 (2017).
[35] L. Schneider, P. Beck, J. Wiebe, and R. Wiesendanger, Sci. Adv. **7**, eabd7302 (2021).
[36] J. Kim, W.-J. Jang, T. H. Bui, D.-J. Choi, C. Wolf, F. Delgado, D. Krylov, S. Lee, S. Yoon, C. P. Lutz, A. J. Heinrich, and Y. Bae, arXiv:2103.09582.
[37] Y. Imai, F. Nabeshima, T. Yoshinaka, K. Miyatani, R. Kondo, S. Komiya, I. Tsukada, and A. Maeda, J. Phys. Soc. Jpn. **81**, 113708 (2012).
[38] J. G. Rodrigo, H. Suderow, S. Vieira, E. Bascones, and F. Guinea, J. Phys.: Condens. Matter **16**, R1151 (2004).
[39] S.-H. Ji, T. Zhang, Y.-S. Fu, X. Chen, X.-C. Ma, J. Li, W.-H. Duan, J.-F. Jia, and Q.-K. Xue, Phys. Rev. Lett. **100**, 226801 (2008).
[40] C. Mier, B. Verlhac, L. Garnier, R. Robles, L. Limot, N. Lorente, and D.-J. Choi, J. Phys. Chem. Lett. **12**, 2983 (2021).
[41] See Supplemental Material at http://link.aps.org/supplemental/10.1103/PhysRevB.104.045406 for the experimental local spectra of single Cr impurity, topography of Cr spin chains as well as details on the DFT calculations, which includes Ref. [54].
[42] M. E. Flatté, Phys. Rev. B **61**, R14920 (2000).
[43] M. E. Flatté and J. M. Byers, Phys. Rev. Lett. **78**, 3761 (1997).
[44] R. C. Dynes, V. Narayanamurti, and J. P. Garno, Phys. Rev. Lett. **41**, 1509 (1978).
[45] E. Herrera, I. Guillamón, J. A. Galvis, A. Correa, A. Fente, R. F. Luccas, F. J. Mompean, M. Garcia-Hernandez, S. Vieira, J. P. Brison, and H. Suderow, Phys. Rev. B **92**, 054507 (2015).
[46] S. V. Eremeev, I. P. Rusinov, I. A. Nechaev, and E. V. Chulkov, New J. Phys. **15**, 075015 (2013).
[47] G. Kresse and J. Furthmüller, Comput. Mater. Sci. **6**, 15 (1996).

[48] J. P. Perdew, K. Burke, and M. Ernzerhof, Phys. Rev. Lett. **77**, 3865 (1996).

[49] M. Steinbrecher, R. Rausch, K. T. That, J. Hermenau, A. A. Khajetoorians, M. Potthoff, R. Wiesendanger, and J. Wiebe, Nat. Commun. **9**, 2853 (2018).

[50] L. Schneider, P. Beck, T. Posske, D. Crawford, E. Mascot, S. Rachel, R. Wiesendanger, and J. Wiebe, Nat. Phys. (2021), doi: 10.1038/s41567-021-01234-y.

[51] L. Schneider, P. Beck, J. Neuhaus-Steinmetz, T. Posske, J. Wiebe, and R. Wiesendanger, arXiv:2104.11503.

[52] D. Sticlet, C. Bena, and P. Simon, Phys. Rev. Lett. **108**, 096802 (2012).

[53] M. Mashkoori, S. Pradhan, K. Björnson, J. Fransson, and A. M. Black-Schaffer, Phys. Rev. B **102**, 104501 (2020).

[54] M. Ruby, F. Pientka, Y. Peng, F. von Oppen, B. W. Heinrich, and K. J. Franke, Phys. Rev. Lett. **115**, 087001 (2015).